Enhancing Reliability in Photonuclear Cross-Section Fitting with Bayesian Neural Networks*

Qian-Kun Sun,[1,2,†] Yue Zhang,[3,‡] Zi-Rui Hao,[3] Hong-Wei Wang,[3,1,2,§] Gong-Tao Fan,[3,1,2] Hang-Hua Xu,[3] Long-Xiang Liu,[3] Sheng Jin,[1,2] Yu-Xuan Yang,[1,4] Kai-Jie Chen,[1,5] and Zhen-Wei Wang[1,2]

[1]*Shanghai Institute of Applied Physics, Chinese Academy of Sciences, Shanghai 201800, China*
[2]*University of Chinese Academy of Sciences, Beijing 100049, China*
[3]*Shanghai Advanced Research Institute, Chinese Academy of Sciences, Shanghai 201210, China*
[4]*School of Physics and Microelectronics, Zhengzhou university, Zhengzhou 450001, China*
[5]*School of Physical Science and Technology, ShanghaiTech University, Shanghai 201210, China*

This study investigates photonuclear reaction (γ, n) cross-sections using Bayesian neural network (BNN) analysis. After determining the optimal network architecture, which features two hidden layers, each with 50 hidden nodes, training was conducted for 30,000 iterations to ensure comprehensive data capture. By analyzing the distribution of absolute errors positively correlated with the cross-section for the isotope ^{159}Tb, as well as the relative errors unrelated to the cross-section, we confirmed that the network effectively captured the data features without overfitting. Comparison with the TENDL-2021 Database demonstrated the BNN's reliability in fitting photonuclear cross-sections with lower average errors. The predictions for nuclei with single and double giant dipole resonance peak cross-sections, the accurate determination of the photoneutron reaction threshold in the low-energy region, and the precise description of trends in the high-energy cross-sections further demonstrate the network's generalization ability on the validation set. This can be attributed to the consistency of the training data. By using consistent training sets from different laboratories, Bayesian neural networks can predict nearby unknown cross-sections based on existing laboratory data, thereby estimating the potential differences between other laboratories' existing data and their own measurement results. Experimental measurements of photonuclear reactions on the newly constructed SLEGS beamline will contribute to clarifying the differences in cross-sections within the existing data.

Keywords: Photoneutron reaction, Bayesian neural network, Machine learning, Gamma source, SLEGS

I. INTRODUCTION

Nuclear information is extracted by a photonuclear reaction using 1 - 30 MeV γ-rays. The photoneutron reaction is an important photonuclear reaction in which the excited atomic nucleus emits one or more neutrons. The measurement of the photoneutron reaction (γ, Xn) cross-section is closely related to the Giant Dipole Resonance(GDR) structure (i.e., resonance energy, width, and contribution of the GDR to the energy-weighted sum rule (EWSR)). According to the Brink-Axel hypothesis [1, 2], the γ-ray strength function obtained from photoneutron cross section is a crucial parameter for calculating the neutron capture cross section, which is relevant to the nucleosynthesis of elements heavier than iron in nuclear astrophysics.

Experimental photonuclear reaction data have been obtained from various types of measurements, including bremsstrahlung and quasi-monoenergetic photons from positron annihilation in flight and, more recently, from Laser Compton Scattering (LCS). Initially, bremsstrahlung beams were developed, and these photon beams were constructed in Russia, Canada, Australia, and Germany[3]. In the 1960's, Lawrence Livermore National Laboratory (LLNL, USA)[4] and Centre d'Études Nucléaires de Saclay (France)[5] base on quasi-monochromatic beams using the positron annihilation in flight technique measure abundant photonuclear reaction data[6]. After the development of new-generation synchrotron radiation facilities and high-power lasers, quasi-monoenergetic γ-ray beams were produced in collisions of laser photons with relativistic electrons, which is referred to as Laser Compton Scattering (LCS)[7, 8]. Now SPring-8 LEPS/LEPS-2(Japan)[9], NewSUBARU BL01(Japan)[10–12], UVSOR-III BL1U(Japan), and HIγS(USA)[13] are running, and the Shanghai Laser Electron Gamma Source(SLEGS) has been constructed in Shanghai Synchrotron Radiation Facility(SSRF) in December 2021[14–20]. The Variable Energy Gamma (VEGA) System at Extreme Light Infrastructure Nuclear Physics(ELI-NP, Romania) [21] and the very compact inverse-Compton scattering gamma ray source (VIGAS) at Tsinghua University[22] will contribute to the future. All these facilities already or will soon measure vast amounts of photoneutron reaction experimental data or photonuclear applications, anticipated in the foreseeable future. The key and challenge of extracting physical information from these data lies in the fact that results measured by different laboratories may vary significantly. For example, ^{197}Au is generally considered to accurately measure (γ, n) reaction cross-section, but there are still differences in the data provided by different laboratories. For ^{59}Co, different laboratories cannot agree on the single-peak and double-peak structures[3]. Therefore, when we seek the physical laws of GDR, the systematic errors arising from dif-

* This work were supported by National key research and development program(No.2022YFA1602404), the National Natural Science Foundation of China(NSFC No.12388102, No.12275338, No.12005280), the Key Laboratory of Nuclear Data foundation (JCKY2022201C152).
† Corresponding author, Qian-Kun Sun, E-mail: sunqiankun@sinap.ac.cn
‡ Corresponding author, Yue Zhang, E-mail: zhangyue2023@sari.ac.cn
§ Corresponding author, Hong-Wei Wang, E-mail: wanghw@sari.ac.cn

ferent γ-ray sources, detectors, and analysis methods in various laboratories cannot be ignored.

The experimental GDR data were fitted with several empirical Lorentzian functions[23], e.g. the Standard Lorentzian model(SLO)[1, 2], the Enhanced Generalized Lorentzian model(EGLO)[24], the Generalized Fermi-Liquid model(GFL)[25], the General Hybrid model(GH)[26], the modified Lorentzian approach(MLO1/MLO2/MLO3)[27], and its simplified version SMLO[28]. For this phenomenological approach, it is necessary to classify the number of GDR peaks in the nucleus using two sets of parameters to describe double GDR peak nuclei. On the other hand, the current micro-theoretical models for nuclear excitation mainly consist of two types, Random Phase Approximation model within the framework of density functional theory(QRPA)[29] and Configuration interaction shell model[30]. Calculations using both approaches require a significant amount of numerical computational resources. Both the phenomenological and microscopic methods mentioned above were used to describe the overall properties of the photoneutron reactions. A nuclear reaction model is required for studying a specific reaction channel. For instance, numerous nuclear reaction codes have been developed based on the HauserFestival statistical model such as the well-known NON-SMOKER[31] and TALYS[32], which are widely utilized in nuclear data and astrophysics research. In this study, data from the TALYS-based Evaluated Nuclear Data Library (TENDL-2021)[33] were used for comparison.

Recently, machine learning has been successfully applied to numerous nuclear physics issues. In particular, following the victory of AlphaGo over humans in 2016, a plethora of studies have emerged at the intersection of machine learning and nuclear physics[34–38]. Machine learning and neural networks have been successfully used to study nuclear structure, such as nuclear masses[39–46], charge radii[47], α-decay half-lives[48], and α-clustering structures[49]. In the field of nuclear reactions, machine learning also has a wide range of applications[50–54]. In Ref. [55], the key parameters of GDR were studied based on a traditional classification neural network and two multitask learning (MTL) neural networks. The training and validation sets were divided into single and double GDR peak nuclei, and different neural networks were used for each set. A similar approach was employed to study the total (γ, Xn) photoneutron yield cross-section based on the Lorentzian function-based BNN (LBNN)[52]. These studies describe the photoneutron production cross-section; however, there are many reaction channels in photoneutron reactions, and the ability to accurately describe each reaction channel is significant for photoneutron experiments. Among these reaction channels, the (γ, n) photoneutron reaction channel constitutes the main part of the (γ, Xn) photoneutron reactions and is one of the more accurately measured channels. Therefore, an accurate description of the (γ, n) photoneutron reaction is essential.

In this study, we employed a suitable Bayesian neural network structure with two hidden layers, each containing 50 hidden nodes, to describe the (γ, n) photoneutron cross-section. The training set consisted of consistent experimental data on photonuclear cross-sections from the EXFOR Database[56]. First, by analyzing the absolute and relative errors compared with the TENDL-2021 database and experimental values, our Bayesian neural network demonstrated reliability. Subsequently, predictions were made for three single GDR peak nuclei (^{127}I, ^{197}Au, ^{207}Pb) and two double GDR peak nuclei (^{59}Co and ^{165}Ho). The results showed good agreement with the experimental values, with both double GDR peak nuclei exhibiting double GDR peak structures. Finally, we compared the prediction results for ^{127}I, ^{165}Ho, and ^{197}Au using Saclay and LLNL as training sets. We believe that selecting a consistent training set is crucial when employing machine learning approaches to study photonuclear reaction cross-sections.

This study relied primarily on standard Bayesian neural networks trained on a consistent experimental dataset to enhance the predictive capabilities of the model. The remainder of this paper is organized as follows: Sect.II describes the mathematical principles of Bayesian neural networks, Sect.III presents the details of model training and prediction, and Sect.IV summarizes the findings.

II. BNN MODEL

We employed a Bayesian neural network(BNN) for machine learning to predict the (γ, n) cross-section. The BNN sets the parameters of the neural network θ as probability distributions, treats the network parameters as prior distributions $P(\theta)$, and utilizes Bayesian statistical relations to learn and obtain posterior distributions $P(\theta|D)$[57],

$$P(\theta|D) = \frac{P(D|\theta)P(\theta)}{P(D)}, \tag{1}$$

where the input data $\boldsymbol{x}_n$ and output data σ_n contribute to the data $D = (\boldsymbol{x}_n, \sigma_n)$. The standard practice for the likelihood function is to assume the form of a Gaussian distribution based on an objective function obtained from a least-squares t of the empirical data. Likelihood function is,

$$P(D|\theta) = \exp(-\chi^2(\theta)/2), \tag{2}$$

here, the objective function is

$$\chi^2 = \sum_n^N \frac{[y_n - \sigma(\boldsymbol{x}_n, \theta)]^2}{\Delta t_i^2 + \Delta\sigma_n^2}, \tag{3}$$

where N is the amount of empirical data, Δt_i^2 is hyperparameters of noise; $\Delta\sigma_n$ is the experimental uncertainty. The BNN output functions $\sigma(\boldsymbol{x}_n, \theta)$ of photoneutron (γ, n) are written according to the network parameters θ:

$$\sigma(\boldsymbol{x}_n, \theta) = a + \sum_{j=1}^{H} b_j \tanh(c_j + \sum_{i=1}^{I} d_{ji} x_i), \tag{4}$$

where $\theta = a, b_j, c_j, d_{ji}$, hidden node number of the hidden layer H, input variable number I, and the activation function is set as the tanh type.

Owing to the high dimensionality of the parameters, computing the posterior distribution $P(\theta|D)$ is difficult. Variational inference is employed to approximate $P(\theta|D)$. Variational inference aims to determine κ such that the distribution $q(\theta|\kappa)$ minimizes the Kullback-Leibler (KL) divergence,

$$\begin{aligned}\theta &= \arg\min \mathrm{KL}\left[q(\theta|\kappa)||P(\theta|D)\right] \\ &= \arg\min E_{q(\theta|\kappa)}\left[\ln\frac{q(\theta|\kappa)}{P(\theta|D)}\right] \\ &= \arg\min E_{q(\theta|\kappa)}\left[\ln\frac{q(\theta|\kappa)P(D)}{P(D|\theta)P(\theta)}\right] \\ &= \arg\min \sum_k [\ln q(\theta|\kappa) - \ln P(\theta^{(k)}) - \ln P(D|\theta^{(k)})].\end{aligned} \tag{5}$$

When employing machine-learning techniques to study experimental data in the past, it was common to use evaluation databases or aggregate data from different laboratories. This practice may have obscured systematic biases in the experimental data, making it difficult to reconstruct the true experimental results. To ensure data consistency, we selected experimental data from LLNL and the Centre d'Études Nucléaires de Saclay (France), which are available in the EXFOR Database[56]. In Tab.1, we have included all experimental data from LLNL as the training and validation sets, removing light nuclei with proton or neutron numbers less than or equal to 20 due to the presence of more complex structures in the light nuclei region. After obtaining the data, we excluded data points where the cross-sectional central value was less than 0.1 mb. During training, we processed the data using min-max normalization, specifically defined as $x_{\mathrm{norm}} = (x - x_{\mathrm{min}})/(x_{\mathrm{max}} - x_{\mathrm{min}})$. Our training set consisted of 40 nuclides, while the validation set included 5 nuclides, resulting in a low ratio of 8:1 for the training and validation sets. The input data types included the number of charges Z, the number of neutrons N, the mass A, and the energy ϵ of the injected γ ray.

III. RESULTS AND DISCUSSIONS

To balance data complexity and computational efficiency, we selected a neural network structure based on the loss function. In Fig.1, two hidden layers were defined and experiments were conducted with each hidden layer having 10, 30, 50, 100, and 300 hidden nodes. All the models were trained on an NVIDIA RTX 5000 Ada GPU with training times of 85, 186, 332, 503, and 1251 s. When the number of hidden nodes was relatively small, the loss function tended to plateau with an increasing number of training iterations before continuing to decrease. When the number of training iterations exceeded 20,000, the loss functions of the neural networks with different numbers of hidden nodes tended to converge. Thus, we used 30,000 iterations with 50 nodes per hidden layer to ensure thorough learning.

To ensure that the neural network is not overfitted, absolute and relative errors are introduced:

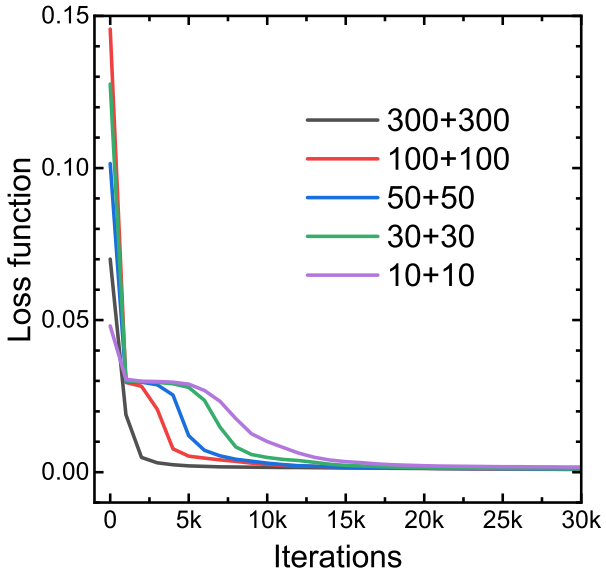

Fig. 1. (Color online) Comparison of the loss function (Mean Squared Error, MSE) deviation for both layers with 10, 30, 50, 100 and 300 hidden nodes. Shown in first + second notes number, respectively

$$\begin{aligned}\delta_a &= \frac{1}{n}\sum_{i=1}^{n}\delta(\boldsymbol{x}_n) \\ &= \frac{1}{n}\sum_{i=1}^{n}|\sigma_{\mathrm{BNN}}(\boldsymbol{x}_n) - \sigma_{\mathrm{exp}}(\boldsymbol{x}_n)| - \delta_{\mathrm{exp}}(\boldsymbol{x}_n),\end{aligned} \tag{6}$$

where $\sigma_{\mathrm{BNN}}(\boldsymbol{x}_n)$ are the BNN predicted values, $\sigma_{\mathrm{exp}}(\boldsymbol{x}_n)$ and $\delta_{\mathrm{exp}}(\boldsymbol{x}_n)$ are the experimental values and errors from LLNL, respectively. In Eq.6, when the absolute difference between the predicted and experimental values $|\sigma_{\mathrm{BNN}}(\boldsymbol{x}_i) - \sigma_{\mathrm{exp}}(\boldsymbol{x}_i)|$ is less than the experimental error $\delta_{\mathrm{exp}}(\boldsymbol{x}_i)$. Here, $\delta(\boldsymbol{x}_i)$ was set to zero. Similarly, the relative error can be expressed as

$$\begin{aligned}\delta_r &= \frac{1}{n}\sum_{i=1}^{n}\frac{\delta(\boldsymbol{x}_n)}{\sigma_{\mathrm{exp}}(\boldsymbol{x}_n)} \\ &= \frac{1}{n}\sum_{i=1}^{n}\frac{|\sigma_{\mathrm{BNN}}(\boldsymbol{x}_n) - \sigma_{\mathrm{exp}}(\boldsymbol{x}_n)| - \delta_{\mathrm{exp}}(\boldsymbol{x}_n)}{\sigma_{\mathrm{exp}}(\boldsymbol{x}_n)}.\end{aligned} \tag{7}$$

A comparison between the BNN predicted values (red curve) and the experimental values (black squares) for the isotope ^{159}Tb in the training set is shown in Fig.2. The neural network accurately predicted the (γ, n) photoneutron cross-section of ^{159}Tb and the energies corresponding to the two GDR peaks. In Fig.2(a), the red dots represent the absolute errors between the predicted values of ^{159}Tb from the BNN and the experimental values. In Fig.2(b), the blue dots represent the corresponding relative errors. It can be observed that the absolute error shows a clear positive correlation with the experimental values, while the relative error does not exhibit a significant positive correlation with the experimental values. This suggests that, although the absolute error increases with

Table 1. The training and validation set, all experimental data were taken from the LLNL or Saclay, available in EXFOR Database[56]

Lab	Author	Training set	Validation set
LLNL	Alvarez	^{55}Mn	^{59}Co
	Berman	^{75}As, ^{89}Y, ^{90,91,92,94}Zr, ^{107}Ag, ^{133}Cs, ^{138}Ba, ^{141}Pr, ^{153}Eu, ^{160}Gd, ^{186}W, ^{186,188,189,190,192}Os, ^{239}Pu,	^{127}I, ^{165}Ho,^{197}Au
	Bramblett	^{159}Tb, ^{181}Ta,	^{127}I
	Caldwell	^{232}Th, ^{235,238}U	
	Harvey	^{206,208}Pb, ^{209}Bi	^{207}Pb
	Fultz	^{51}V, ^{58,60}Ni, ^{63,65}Cu, ^{115}In, ^{116,117,118,119,120,124}Sn	^{59}Co, ^{197}Au
Saclay	Veyssiere	^{51}V, ^{208}Pb, ^{232}Th, ^{238}U	^{197}Au
	Carlos	^{64}Zn, ^{70,72,74,76}Ge, ^{75}As, ^{76,78,80,82}Se, ^{142,143,144,145,146,148,150}Nd, ^{144,148,150,152,154}Sm	
	Lepretre	^{89}Y, ^{90}Zr, ^{93}Nb, ^{103}Rh, ^{115}In, ^{133}Cs, ^{140,142}Ce, ^{116,117,118,120,124}Sn, ^{124,126,128,130}Te	
	Beil	^{92,94,96,98,100}Mo	
	Bergere	^{139}La, ^{159}Tb, ^{181}Ta,	^{127}I, ^{165}Ho

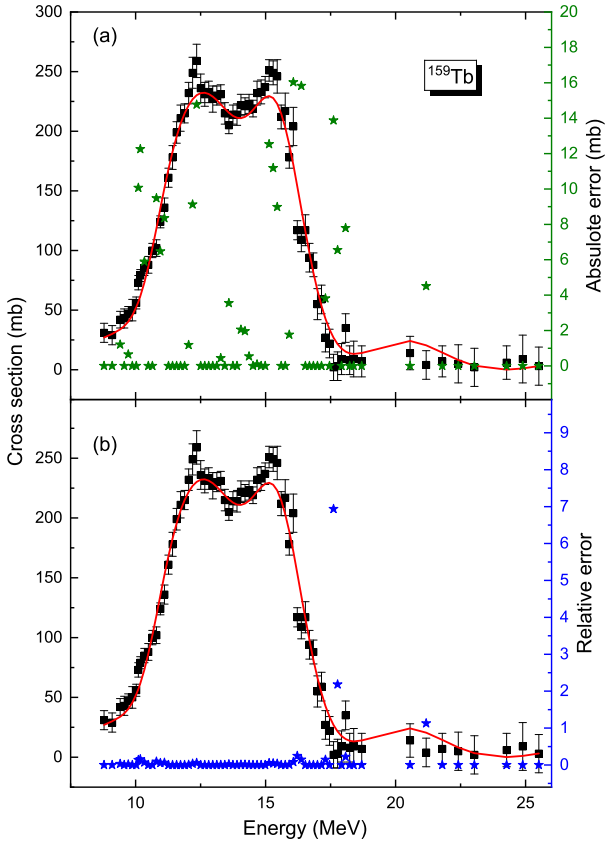

Fig. 2. (Color online) Comparison of the BNN predictions (red curve) and experimental values (black squares) of ^{159}Tb for the training set, along with the absolute(a) and relative errors(b) of each point

the experimental valuesindicating the neural network's ability to capture the magnitude of deviations from the experimental resultsthe relative error does not show a similar correlation. This lack of correlation implies that the performance of the neural network was consistent across different ranges of experimental values, supporting the conclusion that the neural network training did not lead to overfitting.

In past studies of photonuclear reaction cross sections, experimental values from different laboratories or evaluation databases were typically aggregated. The data were then divided into two training sets: one for single GDR peak nuclei and the other for double GDR peak nuclei, facilitating improved learning[55] or similar processing, e.g., employing empirical formulas to control the values of hidden nodes in the output layer[52], to achieve better prediction results for the validation set Without separating these two types of nuclei, the predicted atomic nuclei would exhibit only a single GDR peak. In the present study, the model training did not distinguish between single and double GDR peak nuclei. Various devices used for photonuclear physics experiments employ different γ-ray sources, detector models, and data analysis methods, which can lead to significant discrepancies when measuring the photoneutron yield cross-section of the same nucleus. Notable data discrepancies were observed for 19 nuclei investigated between the LLNL and Centre d'Etudes Nucleaires of Saclay. If the training set consists of experimental values selected from multiple laboratories, systematic errors from these facilities may obscure structural information within the data. Consequently, this study utilized a training set derived exclusively from LLNL experimental data to ensure consistency.

Fig.3 illustrates a macroscopic comparison of the single nuclear mean absolute and mean relative errors on the training set of the BNN, along with the computed results from the TALYS-based Evaluated Nuclear Data Library (TENDL-2021) [33]. Fig.3 depicts the mean absolute and mean relative errors between the BNN's predictions and experimental values from LLNL, as well as those between TENDL-2021 data and the same experimental values. Comparing Fig.3 (a) with Fig.3 (c), the mean absolute errors for single nuclei between the BNN's predictions and experimental values show a uniform distribution. The BNN's minimum single nuclear

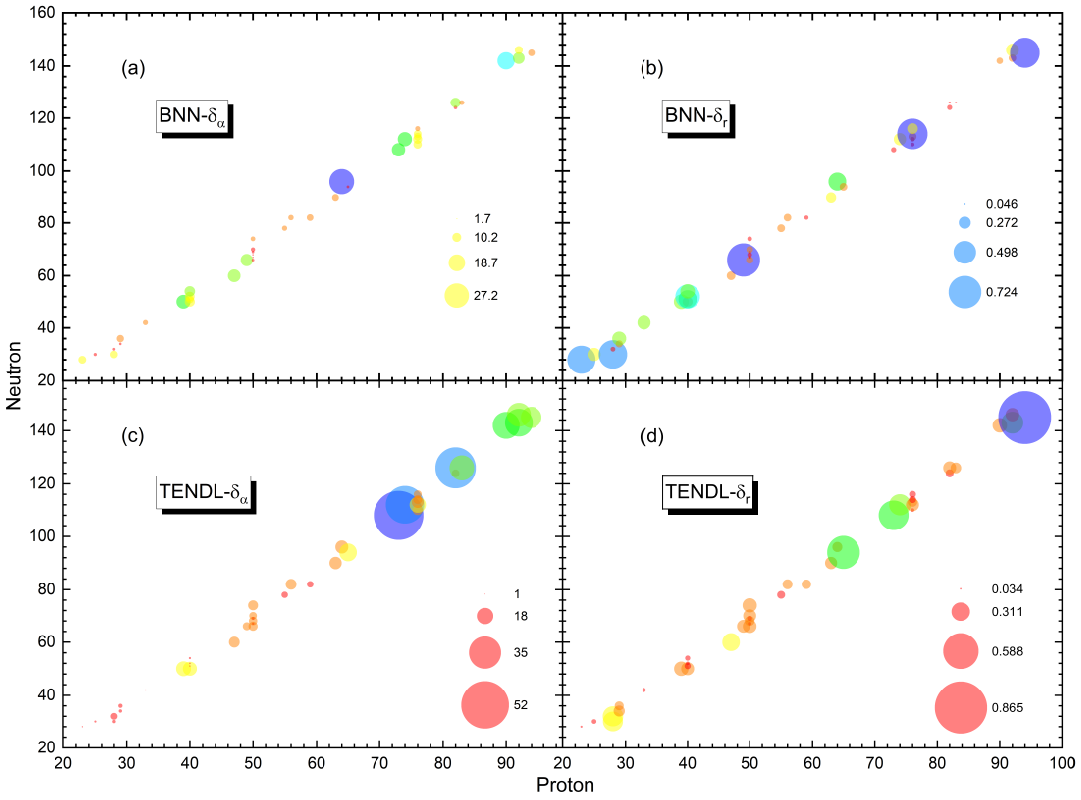

Fig. 3. (Color online) Comparison between the Bayesian neural network's single nuclear mean absolute and mean relative errors on the training set and the computed results from the TALYS-based Evaluated Nuclear Data Library (TENDL-2021)[33]. The values in Fig. (a) and (c) have been normalized according to their respective maximum values; the same processing has also been applied to Fig.(b) and (d)

absolute error is $1.7\,\mathrm{mb}$, which is higher than the $1\,\mathrm{mb}$ reported in TENDL-2021. The overall mean absolute error for single nuclei between the BNN's predictions and experimental values is $7.14\,\mathrm{mb}$, smaller than the $13.56\,\mathrm{mb}$ reported in TENDL-2021. The distribution and minimum values of the single-nuclear mean relative errors are shown in Fig.3 (b) and Fig.3 (d), which lead to conclusions similar to those drawn from the distribution of single nuclear mean absolute errors. Meanwhile, the BNN's minimum single nuclear relative error was 0.046, higher than the 0.034 in TENDL-2021. In contrast, the overall mean relative error of a single nucleus between TENDL and the experimental values is 0.209, which is smaller than the 0.252 for the BNN. Based on the above comparison, it is evident that the BNN demonstrates good predictive ability for the training set.

In Fig.4, the (γ, n) cross-section data for ^{127}I, ^{197}Au, and ^{207}Pb are predicted and compared with experimental values and TENDL-2021 data. Notably, in the experimental measurements, all three nuclei exhibit only one GDR peak. The red curve represents the mean obtained by sampling the posterior distribution of the trained neural network using the Markov Chain Monte Carlo method, with the shaded region indicating a 99% confidence interval. The narrowness of these shaded confidence intervals demonstrates the high accuracy of the BNN in predicting these data. The TENDL-2021 database used for comparison employed linear interpolation to obtain its data.In Fig.4(a), the comparison for isotope ^{127}I is presented. Here, the GDR peak position and width of the (γ, n) photonuclear cross-section predicted by the BNN align well with the experimental values, though the maximum cross-section value is slightly higher than the experimental result. The Giant Dipole Resonance (GDR) is associated with the collective excitation of the nucleus. Additionally, the onset of the photoneutron reaction, marked by the one-neutron separation energy S_{1n}, is crucial in calculating r-process observables. The quality of the high-energy tail description depends on distinguishing between one-neutron (γ, n), two-neutron $(\gamma, 2n)$, and more-neutron reaction channels experimentally. Therefore, accurately describing both low- and high-energy cross-sections is essential. The BNN's ability to accurately describe cross-sections at low energies is promising. In the high-energy tail, BNN predictions were closer to experimental values than the TENDL-2021 database. A comparison for a similar nuclear isotope, ^{197}Au, is shown in Fig.4(b). The BNN predictions align very well with experimental values in terms of GDR peak position, width, and maximum cross-section, whereas the TENDL-2021 database shows some deviation, particularly in width. Both low-energy and high-energy cross-sections are well described by the BNN. In Fig.4(c), the BNN's predictions for the ^{207}Pb isotope are also shown to be highly accurate. The BNN provided an excellent description of the high-energy tail, closely match-

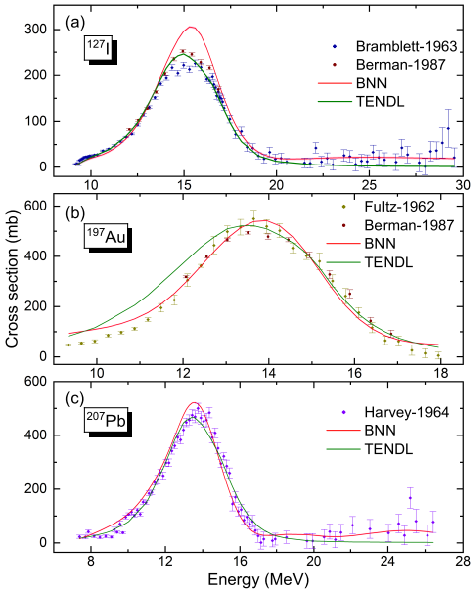

Fig. 4. (Color online) The single GDR peak (γ, n) cross-section data for ^{127}I, ^{197}Au, and ^{207}Pb predicted by the Bayesian neural network (red curve) are compared with experimental data (color dots) and TENDL-2021 data (green curve).

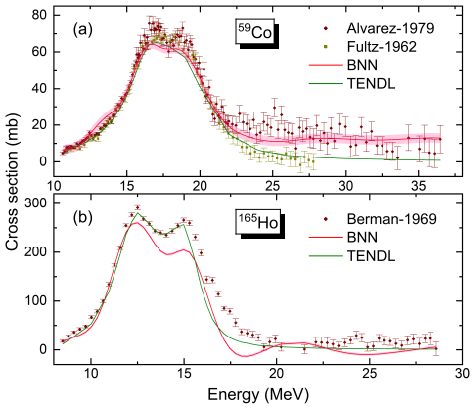

Fig. 5. (Color online) the double GDR peaks (γ, n) cross-section data for ^{59}Co and ^{165}Ho were predicted by the BNN(red curve), which are compared with experimental data(color dots) and the TENDL-2021 data(green curve), respectively.

ing experimental data, including the subtle bump near $\epsilon = 17$ MeV and the rise when $\epsilon > 24$ MeV. These features were not captured by the TENDL-2021 database or in prior BNN-based studies [52]. It is worth emphasizing the significance of the selected nuclei. For ^{207}Pb, the training set included neighboring nuclei ^{206}Pb and ^{208}Pb, which likely explains why the BNN predictions for ^{207}Pb closely match the experimental values. This result is encouraging for predicting cross-section data of unstable nuclei adjacent to stable ones: by measuring the cross-section data of stable nuclei, the neural network can accurately predict the cross-section data of these unstable nuclei. Additionally, ^{127}I and ^{197}Au, whose neighboring mass numbers were not included in the training set, were still accurately described by the BNN. This highlights the strong capability of the BNN to predict the cross-sections of single-GDR-peak nuclei, capturing the GDR shape and both the low- and high-energy tails effectively.

In Fig.5, we also present the BNN predictions for (γ, n) cross-sections for nuclei with double GDR peaks, specifically ^{59}Co and ^{165}Ho. Similar to the comparisons shown in Fig.4, the TENDL-2021 database results are also included for reference. In Fig.5(a), the BNN prediction for the photonuclear cross-section of ^{59}Co accurately reproduces the double GDR peak structure, with peak positions, widths, and maximum cross-section values closely matching experimental data. Additionally, the confidence interval (red shading) for the BNN prediction for ^{59}Co is wider, due to the proximity to the boundaries of the training set, where BNN predictions carry less certainty. The BNN also accurately predicts the onset of (γ, n) cross-sections, aligning well with experimental data. Focusing on the high-energy tail, we note that two sets of experimental data are available from Lawrence Livermore National Laboratory. The BNN prediction aligns well with the dataset measured by Alvarez [58], while the TENDL-2021 database aligns better with the dataset measured by Fultz [59]. For another double GDR peak isotope, ^{165}Ho, shown in Fig.5(b), the BNN predictions demonstrate good agreement with experimental data in terms of peak positions and widths of the cross-section structure. However, the cross-section values for the two GDR peaks are slightly lower than the experimental values, indicating partial agreement. This may be due to limited data near ^{165}Ho in the training set, with neighboring isotopes being ^{160}Gd and ^{181}Tathe latter having a mass number difference of 16 relative to ^{165}Ho. Despite this limitation, the BNN provides a cross-sectional prediction that is still close to the experimental values for both low-energy and high-energy tails. Both ^{59}Co and ^{165}Ho are double GDR peak nuclei, and the BNN's red curves effectively capture the GDR peak positions and lower cross sections in the low- and high-energy tails for these nuclei. Thus, it appears that the BNN does not need to distinguish between single and double GDR peak nuclei when predicting nuclear cross-sections, though additional consistent experimental data may be needed.

Data from Centred'É tudes Nucléaires de Saclay (France) using the same γ-ray source were also included in the BNN training set, as these data are abundant and similar to those from the Lawrence Livermore National Laboratory (LLNL, USA). The training sets are presented in Tab. 1. Three nuclides ^{127}I, ^{165}Ho, and ^{197}Aumeasured by both Saclay and LLNL were selected as the validation set. The BNN's reliability in predicting single- and double-GDR peak nuclei has already been validated. In this study, we focused on comparing the BNN's sensitivity to discrepancies when learning from data generated by different laboratories.In Fig.6, it is notable that the confidence intervals (shaded areas) provided by the BNN, trained on both datasets for these three nuclides, were very narrow. In particular, when using the Saclay training set, the shaded area was nearly imperceptible, even though the central value curve was minimized in thickness in the figure. This may be due to Saclay's more precise measurements.

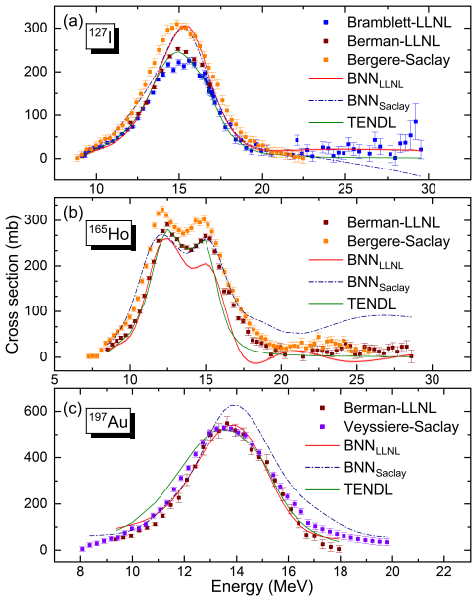

Fig. 6. (Color online) The (γ, n) cross-section data for ^{127}I, ^{165}Ho, and ^{197}Au, predicted by the Bayesian neural network using two training sets: one from Lawrence Livermore National Laboratory (solid red line) and the training set from Centred'É tudes Nucléaires de Saclay (blue dashed line). Predictions are compared with experimental data (colored dots) and TENDL-2021 data (green curve).

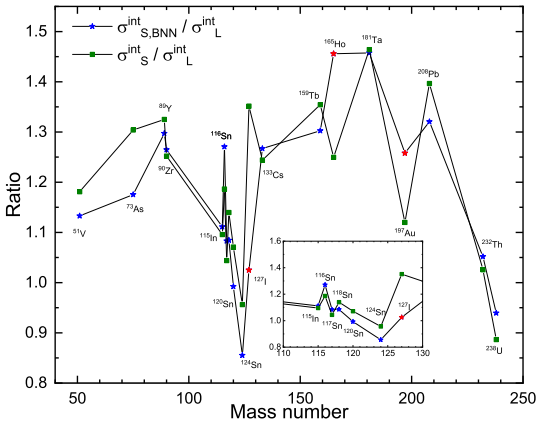

Fig. 7. (Color online) The mean difference between the BNN predictions using Saclay as the training set and LLNL is marked with asterisks; the mean difference within the training set is marked in blue, and in the validation set in red. The mean difference between Saclay and LLNL data is represented by a green square.

In Fig.6(a), it is evident that for ^{127}I, the BNN cross-section predictions based on both Saclay and LLNL data show almost no difference. This similarity arises because the cross-section measurements from the two laboratories for this mass region were consistent. The BNN results for both training sets were similar to Saclay's data, raising questions about the maximum GDR peak value obtained from LLNL for ^{127}I.In Fig. 6(b), the BNN, trained with the Saclay data, also accurately predicted the double GDR peaks of ^{165}Ho. When the Saclay data were used as the training set, the energy corresponding to the first GDR peak matched Saclay's experimental values. Similarly, when LLNL data were used as the training set, the first GDR peak energy aligned with LLNL's experimental values. This highlights the importance of consistency in the training set to enable the Bayesian neural network to accurately predict peak positions. Specifically, if the training set contains data from different laboratories, the predicted peak positions, especially for nuclides with double GDR peaks, may deviate. Fig. 6(c) shows a comparison for ^{197}Au, where the second half of the GDR peak appears considerably higher than the experimental values. This discrepancy arises because nearby nuclides in the training set, ^{181}Ta and ^{208}Pb, have significantly higher values than those obtained from LLNL. However, Saclay's ^{197}Au values were more consistent with LLNL's results.

The ratio $\sigma_X^{\rm int}/\sigma_{\rm L}^{\rm int}$ $(X = {\rm S; S, BNN})$ is shown in Fig. 7, where $\sigma_{\rm S,BNN}^{\rm int}$ represents the BNN predictions based on the Saclay training set, and $\sigma_{\rm S}^{\rm int}$ and $\sigma_{\rm L}^{\rm int}$ are the experimentally integrated cross-sections from Saclay and LLNL, respectively. The integrated cross-sections were obtained following the approach from [3]

$$\sigma_{\rm X,L}^{\rm int} = \int_{E_{\rm min}}^{E_{\rm max}} \sigma_{\rm X,L}(\epsilon){\rm d}\epsilon, \tag{8}$$

where $E_{\rm min}$ is the minimum intersection point of the energy ranges from the two laboratories' γ-ray sources, and $E_{\rm max}$ is the maximum intersection point. The average values $\langle\sigma_{\rm S}^{\rm int}/\sigma_{\rm L}^{\rm int}\rangle$ and $\langle\sigma_{\rm S,BNN}^{\rm int}/\sigma_{\rm L}^{\rm int}\rangle$ were 1.192 and 1.176, respectively. The (γ, n) cross-sections from Saclay are generally higher than those from LLNL, aligning with the conclusions of Ref [60].For the Sn isotope chain, the cross-section data from both laboratories were very similar, as shown in the figures. This consistency led the BNN, trained on either set, to predict cross-section magnitudes comparable to those for ^{127}I, which more closely aligns with the Saclay data. In cross-section measurements for the Sn isotope chain, both laboratories reported peak values between 270 mb and 300 mb. However, for ^{127}I, LLNL recorded a significant decrease to around 220 mb, while Saclay's measurements remained close to 300 mb. Therefore, we consider Saclay's data to be more reliable for peak values. However, regarding peak width measurements, the BNN tended to favor data from LLNL. Given the high consistency between both laboratories' measurements for nearby nuclei, we believe the BNN-predicted values likely approximate the true values. For ^{197}Au, both laboratories produced similar measurements, with a small ratio difference; however, the BNN predicted a slightly larger ratio. Despite this, the larger ratio still reflected the trend of actual differences between the two laboratories. Thus, when trained on a consistent dataset, the BNN effectively captures both individual nuclide trends and the broader systematic features of the training set, making it a valuable tool for comparing laboratory results. Furthermore, the BNN's inherent generalization capability allows it to predict unknown data based on existing laboratory data, estimating potential differences between its predictions and measurements from other laboratories. Due to its robust capability to capture data structures

and generalize across datasets, the BNN can be effectively applied to cross-sections for neutron, proton, and α-particle reaction channels. In cases with sparse experimental data, the BNN can provide reliable predictions for unmeasured values. Conversely, in data-rich scenarios, it can assess data reliability and help identify the most accurate measurements.

IV. SUMMARY

We explored photonuclear reaction cross-sections using BNN analysis. Initially, we optimized the network architecture by examining the behavior of the loss function across various hidden node counts. The optimal configuration comprises two hidden layers with 50 nodes each. Since the loss functions for networks with different hidden-node counts stabilized after 20,000 iterations, we conducted 30,000 training iterations to ensure thorough capture of information from the training set.

we evaluated theTo evaluate training performance and detect potential overfitting, we analyzed both absolute and relative errors. In studying the isotope ^{159}Tb, the BNN predictions yielded a mean absolute error of $3.09\,\mathrm{mb}$ and a mean relative error of 0.169 compared to experimental data. A positive correlation was observed between the absolute error and the experimental values, demonstrating the network's ability to accurately capture data characteristics. However, there was no significant correlation between the relative error and experimental values, indicating that overfitting was not an issue. The predicted results further support this assertion, showing that the BNN performed comparably to the experimental values in the TENDL-2021 database. The BNN had an average absolute error of $7.14\,\mathrm{mb}$ and an average relative error of 0.252, whereas the TENDL-2021 database yielded an average absolute error of $13.56\,\mathrm{mb}$ and an average relative error of 0.209. This confirms that the BNN provides a reliable fit for (γ, n) photonuclear cross-sections.

After training, the BNN made predictions for three single-peak nuclei (^{127}I, ^{197}Au, and ^{207}Pb) and two double GDR peak nuclei (^{59}Co and ^{165}Ho). Comparisons with experimental values and the TENDL-2021 database demonstrated the BNN's ability to accurately predict GDR parameters for nuclei in the validation set. Furthermore, precise predictions in low- and high-energy cross-sectional regionswhere data is sparsehighlighted the BNN's strong generalization capabilities, likely due to the training set's consistency, which primarily consisted of experimental data from Lawrence Livermore National Laboratory.

FinallyIn a secondary analysis, we employed another training set (Saclay) to evaluate the BNN's versatility. We found that this training set could also reliably predict the (γ, n) photonuclear cross-sections for both single- and double GDR peak nuclei. Interestingly, when using data from both laboratories in the training sets, the BNN predictions for ^{127}I more closely matched Saclay's data, whereas the TENDL database aligned more closely with LLNL's data. The training set source also influenced predictions for the first peak in double GDR peak nuclei. For example, for ^{165}Ho in the validation set, the predicted first peak tended to align with the laboratory data used for training. This analysis illustrates that BNNs, when trained consistently on datasets from different laboratories, can estimate unknown data by extrapolating from available laboratory data and can thus reveal potential discrepancies between measurements from different laboratories. In future work, we aim to extend BNN-based studies to include cross-sections for all photonuclear reaction channels using physics-informed machine learning. This approach can provide reliable guidance for precise photonuclear reaction cross-section measurements at the SLEGS beamline. Additionally, we plan to predict cross-sectional data for photonuclear reactions that cannot be measured experimentally, thereby contributing to resolving significant questions regarding element formation in nuclear astrophysics.

Author Contributions: All authors contributed to the study's conception and design. Material preparation, data collection, and analysis were performed by Q. K. Sun. The first draft of the manuscript was written by Q. K. Sun, Y. Zhang and H. W. Wang. All authors commented on the previous versions of the manuscript. All the authors have read and approved the final version of the manuscript.

[1] D. M. Brink, Ph.D. thesis, Oxford University, Oxford, UK (1955)

[2] P. Axel, Electric dipole ground-state transition width strength function and 7-MeV photon interactions. Phys. Rev. **126**, 671–683 (1962). doi:10.1103/PhysRev.126.671

[3] T. Kawano, Y. Cho, P. Dimitriou, et al., IAEA Photonuclear Data Library 2019. Nucl. Data Sheets **163**, 109–162 (2020). doi:10.1016/j.nds.2019.12.002

[4] C. R. Hatcher, R. L. Bramblett, N. E. Hansen, et al., Width of photon line produced by positron annihilation at 15 MeV. Nucl. Instr. Meth. **14**, 337–342 (1961). doi:10.1016/0029-554X(61)90098-2

[5] J. Miller, C. Schuhl, G. Tamas, C. Tzara, Résultats préliminaires sur une source de photons monochromatiques par annihilation en vol de positons. J. Phys. radium **21**, 296–298 (1960). doi:10.1051/jphysrad:01960002105029601

[6] B. L. Berman, S. C. Fultz, Measurements of the giant dipole resonance with monoenergetic photons. Rev. Mod. Phys. **47**, 713–761 (1975). doi:10.1103/RevModPhys.47.713

[7] R. H. Milburn, Electron scattering by an intense polarized photon field. Phys. Rev. Lett. **10**, 75–77 (1963). doi:10.1103/PhysRevLett.10.75

[8] F. R. Arutyunian, V. A. Tumanian, The compton effect on relativistic electrons and the possibility of obtaining high energy beams. Physics Letters **4**, 176–178 (1963). doi:10.1016/0031-9163(63)90351-2

[9] T. Nakano, H. Ejiri, M. Fujiwara, et al., New projects at SPring-8 with multi-GeV polarized photons. Nucl. Phys. A **629**, 559–566 (1998). doi:10.1016/S0375-9474(97)00737-9

[10] H. Ohgaki, H. Toyokawa, K. Kudo, et al., Generation and

application of Laser-Compton gamma-ray at ETL. Nucl. Instr. Meth. A **455**, 54–59 (2000). doi:10.1016/S0168-9002(00)00693-8

[11] S. Amano, K. Horikawa, K. Ishihara, et al., Several-mev γ-ray generation at newsubaru by laser compton backscattering. Nucl. Instr. Meth. A **602**, 337–341 (2009). doi:10.1016/j.nima.2009.01.010

[12] H. Utsunomiya, S. Hashimoto, S. Miyamoto, The γ-ray beamline at NewSUBARU. Nucl. Phys. News **25**, 25–29 (2015). doi:10.1080/10619127.2015.1067539

[13] H. R. Weller, M. W. Ahmed, The HIγS facility: A free-electron laser generated gamma-ray beam for research in nuclear physics. Mod. Phys. Lett. A **18**, 1569–1590 (2003). doi:10.1142/S0217732303011216

[14] Z. Hao, G. Fan, L. Liu, et al., Design and simulation of 4π flat-efficiency ^{3}He neutron detector array. Nucl. Techn **43**, 57–65 (2020)

[15] H. W. Wang, G. T. Fan, L. X. Liu, et al., Commissioning of laser electron gamma beamline SLEGS at SSRF. Nucl. Sci. Tech. **33**, 87 (2022). doi:10.1007/s41365-022-01076-0

[16] Z. R. Hao, G. T. Fan, H. W. Wang, et al., Collimator system of SLEGS beamline at Shanghai Light Source. Nucl. Instr. Meth. A **1013**, 165638 (2021). doi:10.1016/j.nima.2021.165638

[17] H. H. Xu, G. T. Fan, H. W. Wang, et al., Interaction chamber for laser Compton slant-scattering in SLEGS beamline at Shanghai Light Source **1033**, 166742 (2022). doi:10.1016/j.nima.2022.166742

[18] K. J. Chen, L. X. Liu, Z. R. Hao, et al., Simulation and test of the SLEGS TOF spectrometer at SSRF. Nucl. Sci. Tech. **34**, 47 (2023). doi:10.1007/s41365-023-01194-3

[19] L. X. Liu, H. Utsunomiya, G. T. Fan, et al., Energy profile of laser Compton slant-scattering γ-ray beams determined by direct unfolding of total-energy responses of a BGO detector. Nucl. Instr. Meth. A **1063**, 169314 (2024). doi:10.1016/j.nima.2024.169314

[20] Z. R. Hao, G. T. Fan, H. H. Xu, et al., Quasi-monochromatic gamma beam modulation at SLEGS. Radiation Measurements , 107127 (2024). doi:10.1016/j.radmeas.2024.107127

[21] ELI-NP, http://www.eli-np.ro/documents/ELI-NP-WhiteBook.pdf

[22] Y. C. Du, H. Chen, H. Z. Zhang, et al., A very compact inverse Compton scattering gamma ray source. High Power Laser and Particle Beams **34**, 104010 (2022). doi:10.11884/HPLPB202234.220132

[23] S. Goriely, P. Dimitriou, M. Wiedeking, et al., Reference database for photon strength functions. Eur. Phys. J. A **55**, 1–52 (2019). doi:10.1140/epja/i2019-12840-1

[24] J. Kopecky, M. Uhl, Test of gamma-ray strength functions in nuclear reaction model calculations. Phys. Rev. C **41**, 1941–1955 (1990). doi:10.1103/PhysRevC.41.1941

[25] S. F. Mughabghab, C. L. Dunford, A dipolequadrupole interaction term in E1 photon transitions. Phys. Lett. B **487**, 155–164 (2000). doi:10.1016/S0370-2693(00)00792-9

[26] S. Goriely, Radiative neutron captures by neutron-rich nuclei and the r-process nucleosynthesis. Phys. Lett. B **436**, 10–18 (1998). doi:10.1016/S0370-2693(98)00907-1

[27] V. A. Plujko, S. Ezhov, M. Kavatsyuk, et al., Testing and improvements of gamma-ray strength functions for nuclear model calculations. J. Nucl. Sci. Tech. **39**, 811–814 (2002). doi:10.1080/00223131.2002.10875222

[28] V. A. Plujko, I. M. Kadenko, E. V. Kulich, et al., Title of the paper, in: Proceedings of Workshop on Photon Strength Functions Rel. Topics, Prague, Czech Republic, 2007 (2007)

[29] Y. Tian, Z. Y. Ma, P. Ring, Separable pairing force for relativistic quasiparticle random-phase approximation. Phys. Rev. C **79**, 064301 (2009). doi:10.1103/PhysRevC.79.064301

[30] B. A. Brown, W. D. M. Rae, The Shell-Model Code NuShellX@MSU. Nucl. Data Sheets **120**, 115–118 (2014). doi:10.1016/j.nds.2014.07.022

[31] T. Rauscher, F.-K. Thielemann, Astrophysical Reaction Rates From Statistical Model Calculations. At. Data Nucl. Data Tables **75**, 1–351 (2000). doi:10.1006/adnd.2000.0834

[32] A. J. Koning, D. Rochman, Modern nuclear data evaluation with the TALYS code system. Nucl. data sheets **113**, 2841–2934 (2012). doi:10.1016/j.nds.2012.11.002

[33] TENDL, https://tendl.web.psi.ch/tendl2021/tendl2021.html

[34] R. Zhang, B. Wei, D. Zhang, et al., Few-shot machine learning in the three-dimensional Ising model. Phys. Rev. B **99**, 094427 (2019). doi:10.1103/PhysRevB.99.094427

[35] X. C. Ming, H. F. Zhang, R. R. Xu, et al., Nuclear mass based on the multi-task learning neural network method. Nucl. Sci. Tech. **33**, 48 (2022). doi:10.1007/s41365-022-01031-z

[36] T. L. Zhao, H. F. Zhang, A new method to improve the generalization ability of neural networks: A case study of nuclear mass training. Nucl. Phys. A **1021**, 122420 (2022). doi:https://doi.org/10.1016/j.nuclphysa.2022.122420

[37] Y.-G. Ma, L.-G. Pang, R. Wang, K. Zhou, Phase transition study meets machine learning. Chin. Phys. Lett. **40**, 122101 (2023). doi:10.1088/0256-307X/40/12/122101

[38] W. B. He, Q. F. Li, Y. G. Ma, et al., Machine learning in nuclear physics at low and intermediate energies. Sci. China-Phys. Mech. Astro. **66**, 282001 (2023). doi:10.1007/s11433-023-2116-0

[39] H. F. Zhang, L. H. Wang, J. P. Yin, et al., Performance of the Levenberg–Marquardt neural network approach in nuclear mass prediction. J. Phys. G-Nucl. Part. Phys. **44**, 045110 (2017). doi:10.1088/1361-6471/aa5d78

[40] R. Utama, J. Piekarewicz, H. B. Prosper, Nuclear mass predictions for the crustal composition of neutron stars: A Bayesian neural network approach. Phys. Rev. C **93**, 014311 (2016). doi:10.1103/PhysRevC.93.014311

[41] Z. M. Niu, H. Z. Liang, Nuclear mass predictions based on Bayesian neural network approach with pairing and shell effects. Physics Letters B **778**, 48–53 (2018). doi:https://doi.org/10.1016/j.physletb.2018.01.002

[42] Z. M. Niu, J. Y. Fang, Y. F. Niu, Comparative study of radial basis function and Bayesian neural network approaches in nuclear mass predictions. Phys. Rev. C **100**, 054311 (2019). doi:10.1103/PhysRevC.100.054311

[43] X. H. Wu, P. W. Zhao, Predicting nuclear masses with the kernel ridge regression. Phys. Rev. C **101**, 051301 (2020). doi:10.1103/PhysRevC.101.051301

[44] Y. F. Liu, C. Su, J. Liu, et al., Improved naive Bayesian probability classifier in predictions of nuclear mass. Phys. Rev. C **104**, 014315 (2021). doi:10.1103/PhysRevC.104.014315

[45] Z. X. Yang, X. H. Fan, P. Yin, et al., Taming nucleon density distributions with deep neural network. Phys. Lett. B **823**, 136650 (2021). doi:https://doi.org/10.1016/j.physletb.2021.136650

[46] Z. M. Niu, H. Z. Liang, Nuclear mass predictions with machine learning reaching the accuracy required by r-process studies. Phys. Rev. C **106**, L021303 (2022). doi:10.1103/PhysRevC.106.L021303

[47] D. Wu, C. L. Bai, H. Sagawa, et al., β-delayed one-neutron emission probabilities within a neural network model. Phys. Rev. C **104**, 054303 (2021).

doi:10.1103/PhysRevC.104.054303
[48] C. Q. Li, C. N. Tong, H. J. Du, et al., Deep learning approach to nuclear masses and α-decay half-lives. Phys. Rev. C **105**, 064306 (2022). doi:10.1103/PhysRevC.105.064306
[49] J. J. He, W. B. He, Y. G. Ma, et al., Machine-learning-based identification for initial clustering structure in relativistic heavy-ion collisions. Phys. Rev. C **104**, 044902 (2021). doi:10.1103/PhysRevC.104.044902
[50] Z. A. Wang, J. C. Pei, Y. J. Chen, et al., Bayesian approach to heterogeneous data fusion of imperfect fission yields for augmented evaluations. Phys. Rev. C **106**, L021304 (2022). doi:10.1103/PhysRevC.106.L021304
[51] Z. A. Wang, J. C. Pei, Y. Liu, et al., Bayesian evaluation of incomplete fission yields. Phys. Rev. Lett. **123**, 122501 (2019). doi:10.1103/PhysRevLett.123.122501
[52] Y. Y. Li, F. Zhang, J. Su, Improvement of the Bayesian neural network to study the photoneutron yield cross sections. Nucl. Sci. Tech. **33**, 135 (2022). doi:10.1007/s41365-022-01131-w
[53] Q. F. Song, L. Zhu, J. Su, Target dependence of isotopic cross sections in the spallation reactions ^{238}U+ p, d and ^{9}Be at 1 AGeV. Chin. Phys. C **46**, 074108 (2022). doi:10.1088/1674-1137/ac6249
[54] D. Peng, H. L. Wei, X. X. Chen, et al., Bayesian evaluation of residual production cross sections in proton-induced nuclear spallation reactions. J. Phys. G: Nucl. and Part. Phys. **49**, 085102 (2022). doi:10.1088/1361-6471/ac7069
[55] J. H. Bai, Z. M. Niu, B. Y. Sun, et al., The description of giant dipole resonance key parameters with multi-task neural networks. Phys. Lett. B **815**, 136147 (2021). doi:10.1016/j.physletb.2021.136147
[56] EXFOR, https://www-nds.iaea.org/exfor/
[57] R. M. Neal, Bayesian learning for neural networks, Springer Science & Business Media
[58] R. A. Alvarez, B. L. Berman, D. D. Faul, F. H. Lewis, P. Meyer, Photoneutron cross sections for ^{55}Mn and ^{59}Co. Phys. Rev. C **20**, 128–138 (1979). doi:10.1103/PhysRevC.20.128
[59] S. C. Fultz, R. L. Bramblett, J. T. Caldwell, N. E. Hansen, C. P. Jupiter, Photoneutron cross sections for ^{51}V and ^{59}Co. Phys. Rev. **128**, 2345–2351 (1962). doi:10.1103/PhysRev.128.2345
[60] V. Varlamov, B. Ishkhanov, V. Orlin, Experimental and evaluated photoneutron cross sections for Au 197. Physical Review C **96**, 044606 (2017). doi:10.1103/PhysRevC.96.044606